

HIGH TEMPERATURE EFFECTS OF INTENSE LASER EMISSION FOCUSED ON A SOLID TARGET

N. G. BASOV, V. A. GRIBKOV, O. N. KROKHIN, and G. V. SKLIZKOV

P. N. Lebedev Physics Institute, USSR Academy of Sciences

Submitted November 22, 1967

Zh. Eksp. Teor. Fiz. 54, 1073–1087 (April, 1968)

A pulsed plasma (flare) formed by focusing a Q-switched laser on a solid surface is investigated. Methods of optical diagnostics of nonstationary plasma using a 3-nsec ruby laser emission as the light source are described. The results of an investigation of the dynamics of flare expansion into vacuum and into residual gas atmosphere are presented. When the flare expands in gas, a spherically expanding shock wave is seen to form in the gas. The results of measuring electron density distribution in the flare and in the shock wave are given. The results of the experimental investigation are used to determine the basic gas parameters in the shock wave; the velocity of the wave front reaches 2×10^7 cm/sec.

OUR preceding paper^[1] cited the results of investigating a pulsed plasma generated by focusing a high-power laser pulse on the surface of a solid target. This paper deals with a further and more detailed study of the gas dynamic and high-temperature phenomena that accompany the formation of a pulsed plasma ("flare"). The results of such a research can be of significance to various scientific inquiries related to high-temperature physics inasmuch as the rate of energy injection into matter obtainable by focusing a Q-switched laser beam far exceeds the level typical of fast electrical discharge devices. At the present time the flare temperature that has been reached is of the order of tens of electron volts^[1,2]. Investigation of particle emission from the flare shows that strong currents of emitted particles can be used for injection in accelerators^[3]. The flare is a good source of multicharged ion spectra. The preceding papers^[4] reported the discovery of a series of new ion lines with a large effective charge accomplished in the course of investigating the vacuum ultraviolet spectra of multicharged ions produced in the flare. Since the plasma composition is determined by the material of the heated target, the flare can serve as a source of plasma bunches^[5] whose chemical composition is determined by the target material.

1. GAS DYNAMICS OF FLARE HEATING AND EXPANSION

We briefly consider the basic gas dynamic effects that occur when intense laser emission heats the material. A rigorous analysis of this problem is given in^[6,7].

Simple physical considerations^[8] make it clear that the characteristic dimensions of plasma formed by vaporizing the material from the surface of a condensed body are determined by the coefficient of absorption of the incident emission $k(\rho, \epsilon)$. This coefficient is a function of density and temperature (or specific energy) of the plasma.

In a plane one-dimensional case we can assume that $l(t') \sim k^{-1}(\rho', \epsilon')$, where l is the thickness of the plasma layer and ρ' and ϵ' are the density and internal energy at time t' . This condition enables us to bind the density and specific energy by a functional relationship since

the plasma velocity v equals the velocity of sound in the order of magnitude, $v \approx c = [(\kappa - 1) \times \kappa \epsilon]^{1/2} \approx \sqrt{\epsilon}$, and $l(t') \sim \sqrt{\epsilon} t'$:

$$\sqrt{\epsilon} t \approx k^{-1}(\rho, \epsilon). \quad (1)$$

If the absorption coefficient can be expressed by an exponential function of the form

$$k = k_0 \rho^\alpha e^\beta, \quad (2)$$

we can relate density to the internal energy

$$\epsilon \approx (k_0 \rho^\alpha e) ^{-2/(2\beta+1)} \quad (3)$$

Considering that the mass M of the vaporized material is related to density by $M \approx \rho(t) l(t) \approx \rho \sqrt{\epsilon} t$ and using the energy conservation equation

$$M(\epsilon + v^2/2) \approx qt, \quad (4)$$

where q is the incident radiation flux density, we obtain after eliminating ρ from (3)

$$\begin{aligned} \epsilon &\approx (k_0 q^\alpha)^{2/(3\alpha-2\beta-1)}, \quad \rho \approx [(k_0 t)^3 q^{2\beta+1}]^{-1/(3\alpha-2\beta-1)}, \\ M &\approx (k_0^{-2} q^{\alpha-2\beta-1} t^{3\alpha-2\beta-3})^{1/(3\alpha-2\beta-1)}. \end{aligned} \quad (5)$$

In the special case of a completely ionized gas $\alpha = 2$, $\beta = -3/2$, $k_0 = 2.18 \times 10^{29} z^3 (z+1)^{3/2} A^{-7/2} [\text{cm}^5 \text{g}^{-7/2} \text{erg}^{3/2}]$, where z is the ionic charge and A is the gram-atomic weight. We thus have

$$\epsilon \approx k_0^{1/4} t^{1/4} q^{1/4}, \quad \rho \approx k_0^{-3/4} t^{-3/4} q^{1/4}, \quad M \approx k_0^{-1/4} t^{3/4} q^{1/4}. \quad (6)$$

We can readily see that the result obtained in this manner coincides with the result of a more rigorous analysis of the gas dynamic equations describing the vaporization of material in a self-consistent regime^[6,9]. If the gas dynamic parameters in (6) are represented by their values at the interface between the condensed state and plasma, the coefficients 0.97, 0.31, and 0.37 respectively must be introduced in (6).

The above analysis applies to the plane one-dimensional gas dynamic motion. When a strongly focused beam is used a self-consistent regime is not possible because of the strong and practically spherical expansion of plasma and the correspondingly rapid drop of density in the periphery so that the plasma becomes transparent.

The previous paper^[1] dealt with the qualitative analysis of the problem of heating and expansion of plasma in the spherical case. In a more correct approach to the problem Nemchinov^[10] showed that the spherical expansion and the attendant transparency of peripheral regions of the plasma result in an asymptotically stationary motion determined by the condition $l(\rho, \epsilon) \approx d$ where d is the radius of the focal spot. We then have

$$dk_0 \rho^\alpha e^\beta \approx 1. \quad (7)$$

On the other hand the energy flow passing across a surface situated at a distance d from the target surface is equal to

$$\frac{dM}{dt} \left(\epsilon + \frac{p}{\rho} + \frac{v^2}{2} \right) = Q, \quad (8)$$

where $Q = \pi d^2 q$ is the total radiation flux and dM/dt is the mass flow determined by

$$dM/dt = \pi d^2 v \rho. \quad (9)$$

Setting v equal to the velocity of sound, $v = [(\kappa - 1)\kappa \epsilon]^{1/2} \approx \epsilon^{1/2}$, ($\kappa \approx 5/3$), we obtain

$$\rho \approx Q / 2\pi d^2 \epsilon^{3/2},$$

Finally, using (9) we have

$$\begin{aligned} \epsilon &\approx [(2\pi)^\alpha k_0^{-1} d^{2\alpha-1} Q^{-\alpha}]^{2/(2\beta-3\alpha)}, \\ \rho &\approx \frac{Q}{2\pi d^2} [(2\pi)^\alpha k_0^{-1} d^{2\alpha-1} Q^{-\alpha}]^{-3/(2\beta-3\alpha)}, \\ M &\approx \pi d^2 [(2\pi)^\alpha k_0^{-1} d^{2\alpha-1} Q^{-\alpha}]^{-2/(2\beta-3\alpha)} t. \end{aligned} \quad (10)$$

In particular when $\alpha = 2$ and $\beta = -3/2$ (completely ionized gas)

$$\epsilon \approx 0.45 k_0^{5/4} d^{-5/4} Q^{1/4}, \quad \rho \approx 0.53 k_0^{-1/4} d^{-1} Q^{1/4}, \quad M \approx 1.1 k_0^{-3/4} d^{3/4} Q^{1/4} t, \quad (11)$$

where the numerical coefficients have approximate values.

In conclusion we evaluate the time t_2 beyond which the self-consistent regime describing motion in the plane one-dimensional case is transformed into a regime determined by the spherical character of the motion. According to (5) and (11) we have in the first case

$$\epsilon \approx k_0^{5/4} q^{1/4} t^{1/4}, \quad (12)$$

and in the second case

$$\epsilon \approx k_0^{5/4} q^{1/4} d^{3/4}. \quad (13)$$

Equating the quantities ϵ in (12) and (13) we obtain

$$t_2 \approx k_0^{-1/4} q^{1/4} d^{3/4}.$$

Setting $Q \approx 10^9 \text{ w}$, $q \approx 10^{12} \text{ W/cm}^2$, and $d \approx 2 \times 10^{-2} \text{ cm}$ we arrive at $t_2 \approx 10^{-9} \text{ sec}$. This time is approximately by an order of magnitude shorter than the effective time of the laser pulse which is about 10^{-8} sec . These time intervals however become comparable when the focal spot is large. Furthermore since the internal energy is weakly dependent on time, the use of (12) for $\tau/t_2 \approx 10$ results in a deviation of only $10^{1/4}$ from the value obtained with (13), which is a factor of about 1.8.

2. THE EXPERIMENTAL SETUP

The target was heated by a focused beam of a neodymium laser (Fig. 1). The laser oscillator contained a single rod $15 \times 240 \text{ mm}$. The oscillator pulse was am-

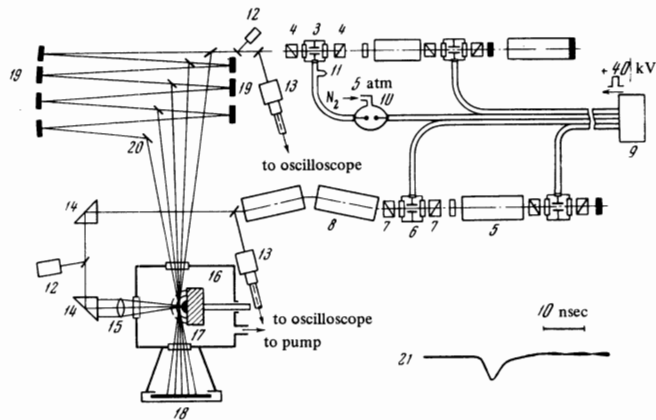


FIG. 1. Diagram of experimental setup for the generation and investigation of pulse plasma. The plasma is formed by focusing a neodymium laser beam in a giant pulse mode on a solid surface: 1—gas laser; 2—ruby laser with Kerr cell control; 3—light pulse sharpening shutter; 4, 7—Glan prism polarizers with air gap; 5—neodymium laser oscillator with Kerr cell control; 6—decoupling cell; 8—neodymium laser amplifiers; 9—square-wave generator; 10—pulse sharpening air gap; 11—matching transmission line; 12—calorimeters; 13—coaxial photocells; 14—total-internal-reflection prisms; 15— $f = 140 \text{ mm}$ lens; 16—vacuum chamber; 17—solid target; 18—photographic plate; 19—light delay line mirror system; 20—optical splitter wedges; 12—oscilloscopic trace of emission pulse after pulse sharpener 3.

pplified by two amplifiers; the first employed a $15 \times 240 \text{ mm}$ rod and the second a $20 \times 240 \text{ mm}$ rod. Each rod was pumped by four IPF-5000 lamps. The rods were water cooled. The oscillator was isolated from the amplifier by a Kerr cell synchronized with the oscillator cell. The same Kerr cell was also used to sharpen the leading edge of the pulse. The ends of the amplifier rods were cut at an angle of $1.5-2^\circ$ to the axis. The maximum pulse energy of the laser emission was 15 J for a pulse length less than 15 nsec. A system of neutral filters controlled the pulse energy while retaining its shape. The energy of the driving oscillator was 1 J; after the first amplifier the energy reached 5 J. The pumping time controlled by an electronic delay circuit was adjusted with respect to the energy maximum and amounted to $350 \mu\text{sec}$. Without the pulse-sharpening cell, the continuous generation background preceding the giant pulse reached 2 J at the output of the last amplifier, amounting to about 20% of the total energy. The emission of the neodymium laser was focused by a lens into a vacuum chamber whose pressure could be adjusted from 2×10^{-6} to 50 mm Hg. The focal spot area was $\sim 10^{-3} \text{ cm}^2$.

A ruby laser employing a crystal of 12 mm diameter and 120 mm length was used to photograph the flare. An IFK-15000 helical lamp was used for pumping and a Kerr cell served as the Q-switch; the laser was water cooled. The pulse length of the ruby laser was 20 nsec. When such a pulse is used to illuminate plasma the pulse length determines the photographic exposure. Given an expansion rate of the plasma edge of $\sim 10^7 \text{ cm/sec}$ and a characteristic dimension of several millimeters, the spatial resolution turned out to be low amounting to $\sim 2 \text{ mm}$. Consequently the ruby laser beam was sharpened by a polarizer and a special Kerr cell designed so as to provide a sufficient electrical pulse voltage amplitude to rotate the polarization plane at least by π . Such

a shutter thus opens and closes in the time it takes for the leading edge of the driving pulse to pass.

The preparation of a highly transmitting cell is very difficult. In our case the transmission of the cell did not exceed 30% not counting absorption in nitrobenzene. A shortening of the pulse length causes a sharp drop of transmission caused apparently by a nonuniform distribution of the electric potential at the electrodes due to the skin effect. Since the pulse sharpening reduced the pulse length by more than an order of magnitude and the amplitude was reduced by a factor of three, the total pulse energy of the ruby laser decreased more than 30 times after sharpening.

The radiation energy that is able to pass through a closed sharpening shutter should not exceed several percent and should be less than 1% if photometry is required. Consequently the polarizers are subject to a rigid requirement: when closed they should attenuate incident radiation by a factor of at least 10^4 . To achieve this we placed two polarizers made of Glan prisms with an air gap on each side of the Kerr cell in the sharpening shutter.

All four Kerr cells were controlled by a single coaxial cable square-wave generator^[11]. The rectangular pulse was formed by five sections of an RK-103 coaxial cable 20 m long. The lengths of the sections forming the transmission line could be adjusted according to experimental requirements and the relative distribution of the synchronizing pulses sent to the Kerr cells was completely determined by the length of the transmitting cable sections. The commutator was a specially designed three-electrode six-channel discharge gap containing two gaps in nitrogen under the pressure of several atmospheres. The leading edge of the electrical pulse was 5 nsec long. The edge of the driving pulse was then shortened by ~1 nsec yet another discharge gap and allowed to enter the optical sharpening shutter. A matching cable section 1 m long was placed at the end of the transmission line beyond the sharpening shutter. The shape of the pulse fronts was observed with an oscilloscope and a capacitive divider. The optical sharpening shutter in the ruby laser beam designed in the above manner was capable of shortening the light pulse from 20 to 3 nsec measured at the half-intensity level.

The electrical pulse amplitude was 19 kV; this was doubled to 38 kV at the neodymium laser cell through reflection. Both lasers employed identical Kerr cells (plate area was 10 cm^2 and plate separation was 1.25 cm). Since the Q-switches of the ruby and neodymium lasers required driving pulses of different amplitude, the electrical pulse at the Kerr cell of the ruby laser was shaped by the noninductive coaxial divider situated directly at the cell (not shown in the diagram).

The emission of the ruby laser was split into five beams by a system of mirrors and optic wedges. The beams intersected within the flare region at small angles. The photographic plate behind the flare was placed far enough to allow the beams to diverge again and thus to avoid overlaps between the photographic images. The optical path length was different for each beam from the laser to the flare. Consequently we secured a time delay of the photographic frames with respect to the beginning of the neodymium laser pulse. The film recorded five frames with shadow flare images at different

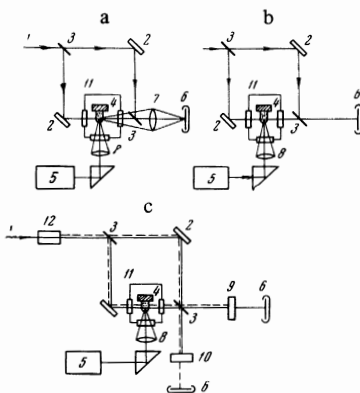


FIG. 2. Three variants of an optical system based on the Mach-Zener interferometer for measuring particle density in plasma: a—flare 4 is projected on film 6 with lens 7; b—superposition of shadow and interferometric photography; c—interferometric photography at two wavelengths: $\lambda_1 = 6943 \text{ \AA}$ and $\lambda_2 = 0.5 \lambda_1$. 1—ruby laser beam after pulse sharpener 3 (see Fig. 1); 2—reflecting mirrors; 3—beam splitters; 5—neodymium laser; 8—lens focusing neodymium laser beam on target 4; 9—light filter for λ_1 ; 10—light filter for λ_2 ; 11—vacuum chamber; 12—nonlinear element (KDP crystal) separating the second harmonic of the ruby laser.

time instants. The frame exposure was equal to the sharpened ruby laser pulse, i.e., 3 nsec and the time interval between frames was chosen at ~50 nsec (or more precisely, beginning with the first in order, 53.1, 51.8, 50.0, and 57.0 nsec). On all the shadowgraphs (Figs. 3, 7, and 8) the direction of the neodymium laser is from left to right and that of the ruby laser is normal to the paper; the frame diameter is 22 mm, the fifth frame is in the center, a carbon target is used, and the frames are designated by numbers.

The ruby laser beam was also used in high-speed interferometric photography. Figure 2a shows the setup for measuring electron density distribution in the expanding plasma used in the experiment; the method is based on the Mach-Zener interferometer. A slight modification of this system (Fig. 2b) permitted us to superimpose the interference pattern with the shadow image of the object. The shadow was obtained in the region of high gradients of electron density where the film was unexposed because of the deflection of the corresponding beams. This may create additional interference bands surrounding regions with large inhomogeneities. These bands are readily recognized because their shape is similar to that of the sharp plasma boundary while the remaining bands have mostly linear structure.

The method of passing a laser beam through plasma can also be used in two-beam interferometry to determine the dispersion of the refraction index as well as its value. The system illustrated in Fig. 2c makes it possible to take photographs simultaneously at two frequencies. The first frequency corresponds to that of the ruby laser beam, while the second equals the second harmonic of the ruby laser separated out by a nonlinear element^[12].

A schlieren method^[13] was used to determine the width of the compression shock in the shock wave; the above ruby laser was used as the light source. Photometric processing of the schlieren photographs yields

the distribution of the index of refraction gradient in the plasma in the direction perpendicular to the knife edge. This method is more convenient in the investigation of processes of the strong shock wave type^[14] characterized by sharp density variations. The sensitivity of this method is higher in this case than that of the interference method and is determined by the expression

$$\frac{\Delta I}{\Delta(\text{grad } n)} = \frac{f}{D} \xi,$$

where ΔI is the change in the relative illumination of the screen, D is the width of the light beam that is allowed to pass over the optical knife edge, f is the focal length of the schlieren lens, ξ is the length of the optical path in the investigated plasma, and n is the index of refraction.

3. FLARE EXPANSION INTO VACUUM

The plasma flare was formed by focusing the neodymium laser beam on the surface of a carbon target (Fig. 1) placed in a vacuum chamber. The emission energy in a single pulse was 10 J. When the decoupling cell was used the half-power pulse length was 12 nsec and the pulse rise time was 4 nsec. Figure 3 shows a five-frame shadowgraph of flare expansion into vacuum. The first two frames show a rapid expansion of the opaque region proceeding at the velocity of 3×10^6 cm/sec. The motion of this region is slowed down to a full stop in frame 3. The dark nucleus has a sharp boundary surrounded by interference rings indicating a high gradient of the index of refraction. The fifth frame shows the breakdown of the opaque region. The refracted rays are visible beyond the target in the form of light bands. The sign of the refraction indicates the appearance of regions in which electron density de-

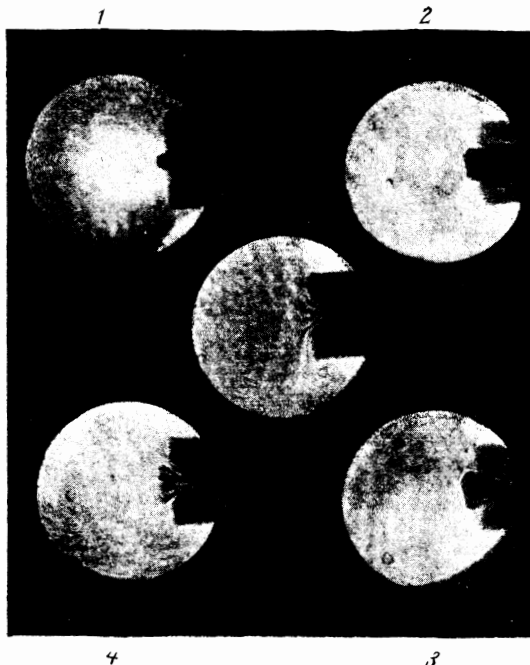


FIG. 3. Five-frame shadowgraph of flare expansion into vacuum. The first frame corresponds to the maximum emission of the neodymium laser.

FIG. 4. Flare shadowgraph photographed with a lens eliminating refraction in the shadow formation.



creases in the direction of the target surface. This seems to be due to the low temperature of matter in these regions.

Knowing the angle of deflection we can estimate the order of magnitude of the electron concentration gradient from the relationship $dn/dx = \alpha n/\xi$ where n is the index of refraction, α is the angle of deflection of the illuminating beam, and the x axis is normal to the target surface. In the case of the third frame, for $\alpha \approx 2 \times 10^{-2}$, $\xi \approx 1$ cm, and $n \approx 1$ we obtain $dn/dx \approx 2 \times 10^{-2} \text{ cm}^{-1}$. Using the expression for the plasma index of refraction we obtain an estimate for the electron concentration gradient

$$\left| \frac{\partial N}{\partial x} \right| = \frac{m\omega^2}{2\pi e^2} \left| \frac{\partial n}{\partial x} \right| \approx 10^{20} \text{ cm}^{-4}, \quad (14)$$

where e and m are the charge and mass of electron respectively and ω is the cyclical frequency of emission of the ruby laser. The shadowgraphs also show that the expansion of material has a jet nature during the final stages. The presence of a large gradient of the index of refraction precludes the appearance of a direct image of the true opaque region in the shadowgraphs. To record this region a lens collecting the flare-reflected rays in the film plane is placed behind the target. A typical photograph corresponding to the third frame of the shadowgraph in Fig. 3 is given in Fig. 4. The photograph indicates that the velocity of the opaque region is $\approx 5 \times 10^5$ cm/sec.

On the other hand according to^[1] the rate of expansion of hot plasma exceeds 10^7 cm/sec in this case and the linear dimensions of the flare are of the order of 1 cm at the time instant corresponding to frame 3. The absence of significant absorption in the "hot" region is due to the fact that at the recording time plasma density has significantly decreased because of expansion. This is further confirmed by the interference pattern shown in Fig. 5 and its analysis (Fig. 6). The appearance of an opaque region in a relatively cold and dense material can be explained by expansion due to a short pressure pulse ("short-time impact"^[15]). The value p of pressure can be determined from (5) and (10), while the characteristic average value is $\bar{p} \approx q/\bar{c}$, where \bar{c} is the mean velocity of sound in the vaporized material. Assuming for the sake of the evaluation that $q \approx 10^{12} \text{ w/cm}^2$

FIG. 5. Interference pattern of a flare expanding into vacuum at a stage corresponding to the third frame (see Fig. 3).



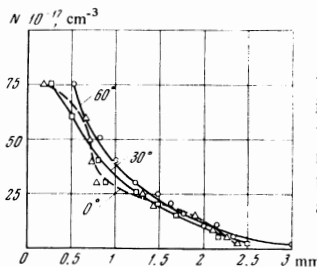


FIG. 6. Electron density distribution in the flare during flare expansion into vacuum in various directions relative to the laser beam axis (curves are marked with angles). The distance from the beam focal point is laid off along the axis of abscissas.

and $\bar{c} \approx 10^7 \text{ cm/sec}$, we obtain $p \approx 10^6 \text{ atm}$. During the expansion of the material that was subject to dynamic compression of this magnitude a partial or even complete vaporization is possible^[16]. Ejection and breaking of the material may also be possible.

The expansion of transparent plasma can be recorded by placing the target in a rarefied gas atmosphere that, incidentally, can be formed by vaporizing the target material by the quasi-continuous background light generation preceding the giant pulse. This can be accomplished by increasing the laser pump power and removing the decoupling Kerr cell (Fig. 1). The continuous generation background with a flux density of $\sim 10^7 \text{ W/cm}^2$ creates a cloud of vaporized material with a particle density of $\sim 10^{17}-10^{18} \text{ cm}^{-3}$ and dimensions of the order of several $\text{cm}^{[17]}$. In this case the expanding hot plasma created by the giant pulse gives rise to a shock wave propagating in the atmosphere of the vaporized material.

Figure 7 shows a shadowgraph corresponding to a single pulse energy of $\sim 10 \text{ J}$ and a quasi-continuous radiation energy of $\sim 3 \text{ J}$. The second, third, and fourth frames clearly show the shock wave with a sharply defined front and a large electron concentration gradient. The front velocity is $1.4 \times 10^7 \text{ cm/sec}$ in the direction parallel to the beam and $1.2 \times 10^7 \text{ cm/sec}$ in the direc-

tion normal to the beam. If we consider that in its final stages the shock wave motion follows the well-known behavior of point explosion^[18], the shock wave velocity corresponds to gas density behind the front of the order of magnitude of $\sim 10^{17} \text{ cm}^{-3}$. The dynamics of motion of the opaque region remains as before.

The vaporization of materials with a low heat of sublimation is so high that the vapor density exceeds 10^{18} cm^{-3} . In this case the gas motion is accompanied by a well developed turbulence leading to a significant distortion of the front shape. Moreover such a high density can cause a local breakdown of the vaporized material.

It follows from our investigation of the flare expansion into vacuum that the presence of the continuous background generation preceding the giant pulse creates conditions that can prove useful in the study of thermodynamic properties of vapors of various materials. For example, we can study the properties of vapors of difficult-to-sublimate materials under high pressures and temperatures corresponding to a shock wave with front velocity of the order of $2 \times 10^7 \text{ cm/sec}$. The initial vapor pressure near the target can be controlled by selecting the vaporization regime. The advantage of such an experiment is the fact that the study of the properties of materials does not require cumbersome installations designed for high pressures and temperatures.

4. SHOCK WAVE FORMATION

At the end of the giant laser pulse the flare assumes the dimension of $\sim 0.2 \text{ cm}$. After the end of the pulse the plasma expands adiabatically. The target surface forms a symmetry plane and in this case the motion would be precisely spherically symmetric if the angular distribution of the initial velocity were uniform. However the velocity of the material at the target is mainly directed normal to the target surface in the process of vaporization. Hence it is clear that a plane target introduces some asymmetry into plasma motion even at a late stage of the expansion. The expansion velocity normal to the surface should be larger than that parallel to the surface and it is so observed in the experiment. The material heated by a single pulse in the atmosphere of residual gas (air at 2 mm Hg) expands and forms a shock wave whose shadowgraph was given previously^[14] for the case of a carbon target. The motion of a shock wave front resembles a strong point explosion in a homogeneous atmosphere^[18].

The material parameters in a strong shock wave are determined for a given equation of state by the initial gas density and front velocity. Gas pressure behind the front is given by

$$p_2 \approx \left(1 - \frac{1}{\beta}\right) \rho_1 D_y^2, \quad (15)$$

where β is compression, ρ_1 is the density of unperturbed gas, and $D_y = 1.8 \times 10^7 \text{ cm/sec}$ is the front velocity. When $\rho_1 = 2.6 \times 10^{-3} \rho_0$, where ρ_0 is air density under normal conditions and $\beta \approx 10$, pressure turns out to be $p_2 \approx 10^3 \text{ atm}$.

The shock wave velocity is weakly dependent on the target material. When gas pressures are high we always observe a strong turbulence of the heated gas and a decrease in the front velocity. Figure 8 shows a shadowgraph of a shock wave at a pressure of 37 mm. There is

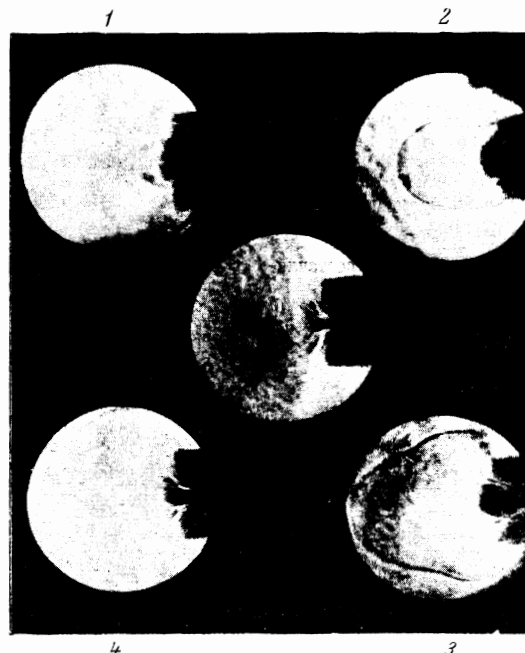


FIG. 7. Five-frame shadowgraph of flare in vacuum without decoupling cell 6 (see Fig. 1). First frame corresponds to the end of the neodymium laser emission pulse.

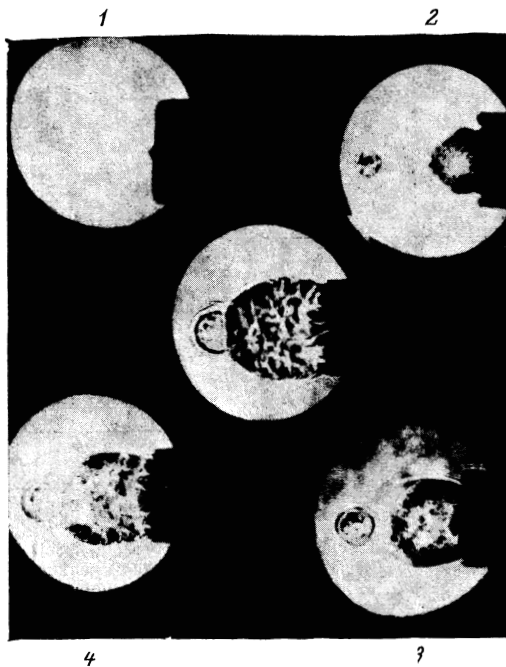


FIG. 8. Five-frame shadowgraph of a shock wave in air (pressure 37 mm Hg) formed during flare expansion from carbon target.

a breakdown in front of the target absorbing a considerable portion of the incident energy.

5. DENSITY DISTRIBUTION BEHIND THE WAVE FRONT

The electron density distribution was experimentally measured in this work by the interference method 90 nsec after the end of the laser pulse. Typical interference patterns of the shock wave are given in Figs. 9a and b for various values of air. With the usual method of photographing the interference patterns, as seen from the figure, within the pressure range of ~ 1 mm Hg the shock wave front weakly perturbs the band image and in some cases the shift is less than a single band, mak-

ing it difficult to analyze the pattern and measure the front coordinates. Therefore a system (see Fig. 2b) of simultaneous superposition of the interference pattern with the shadowgraph was used at low pressures for a qualitative analysis of the interference patterns. Due to light refraction darkened bands appear on film at the sites of large electron density gradients within the compression shock (Fig. 9c, d). The exposure was selected so as to make the darkening clearly visible without disrupting the bands. When pressure exceeds 100 mm Hg light refraction in the compression shock causes a complete darkening of the bands and the method loses its effectiveness.

The interference patterns of the type shown in Fig. 9a and c were analyzed quantitatively. It was assumed that the shock wave has a cylindrical symmetry about the axis of the laser beam. A similar method of analyzing interference patterns was used by Dolgov and Mandel'shtam^[19] to study the shock wave from an electric spark as a source of the illumination pulse although this limited the time resolution to the value of the exposure of $\sim 0.2 \mu\text{sec}$.

Since in reality the wave front deviates somewhat from the axially symmetric form the band displacement chart was plotted by averaging over the points symmetric about the beam axis. The distribution of the index of refraction was analyzed by a method described in^[20] at 1 mm intervals using nine coefficients. The portion of the shock front that moved toward the lens was analyzed at 0.5 mm intervals. In the transverse direction the entire wave volume was sectioned every 0.5 mm.

Figure 10 shows an electron density chart section that passes through the beam axis. The chart also indicates the directions corresponding to the density distribution curves shown in Fig. 11a and b along the radius with the origin at point 0'. This point has no physical interpretation and is selected from geometrical considerations. The front velocity is lower in the direction normal to the laser beam than in the parallel direction. The electron concentration behind the front is also lower in a corresponding manner.

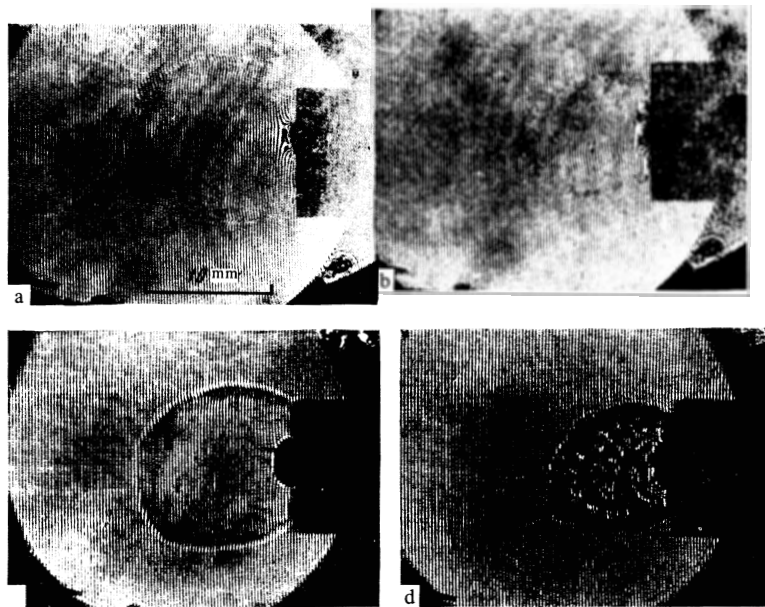


FIG. 9. Interference patterns of a shock wave in air. Frames a, b, c, and d correspond to pressures of 2, 20, 0.93, and 15.3 mm Hg respectively. Frames c and d are obtained by superposing shadow and interferometric photography.

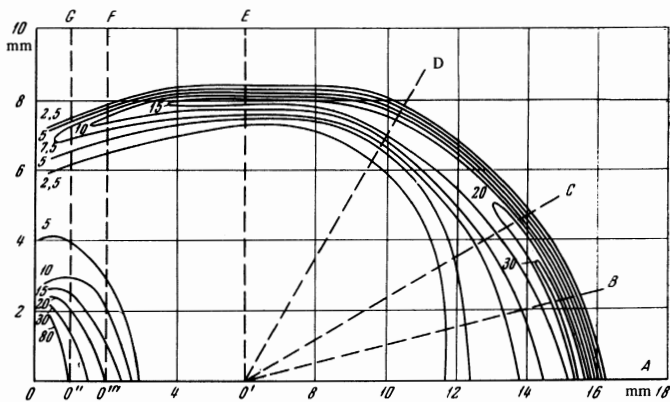


FIG. 10. Chart of constant electron density lines in a shock wave in units of 10^{17} cm^{-3} . Dashed lines denote directions corresponding to shock wave density profiles shown in Fig. 11 a and b.

It follows from the interference patterns that the electron concentration behind the compression shock averaged over a distance of $\sim 1 \text{ mm}$ amounts to $4 \times 10^{18} \text{ cm}^{-3}$ when the front velocity is $\sim 1.8 \times 10^7 \text{ cm/sec}$ and the initial atomic density is $1 \times 10^{17} \text{ cm}^{-3}$. According to the results obtained by Kuznetsov^[21] the shock wave compression is $\beta \approx 8$ at this velocity and weakly depends on temperature. Hence we find that the effective ionic charge in the parallel direction behind the compression shock is $z \approx 5$ and the temperature $kT \approx 40 \text{ eV}^1$. The maximum plasma temperature behind the shock wave front due to a $\sim 4 \text{ GW}$ laser emission was $\sim 100 \text{ eV}$.

Analysis of the ionization processes leading to the establishment of thermodynamic equilibrium in the shock wave shows that the typical dimensions prevailing in our case the ionization equilibrium is not complete and the effective ionic charge is equal to $z \approx 5$. With regard to the hydrogen atmosphere we should expect a complete ionization behind the front on the one hand, and a deviation of the ion temperature from the electron temperature, on the other, since the ions have not enough time to transfer their energy to the electrons during the 10^{-7} sec (for a gas density of $\sim 10^{17} \text{ cm}^{-3}$) typical of the process.

The interference patterns are difficult to use in finding the width of the compression shock because of the heavy demands imposed on the optical elements and the unreasonably cumbersome mathematical computations. Therefore the method of schlieren photography in the laser beam was used to record the shock wave front. The schlieren photographs of the flare and the shock wave are given in Fig. 12. The photographs were taken with the optical knife parallel to the target surface. The measurements indicate that the width of the compression shock is 0.6 mm at a gas pressure of 1 mm ; when the pressure increases the width decreases in approximately inverse proportion to pressure and when the latter exceeds 4 mm Hg the width drops below 0.3 mm and thus beyond the limits of sensitivity of the method determined in this case by the duration of the exposure.

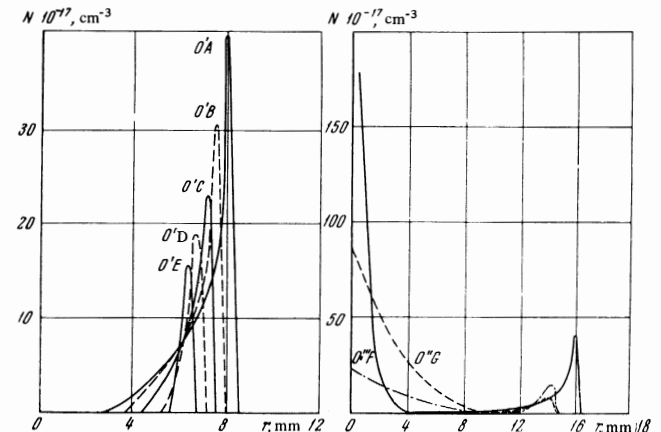


FIG. 11. Electron density profiles in a shock wave (see Fig. 10). Directions corresponding to each profile are marked above the curves. a—distance from point O laid off along the axis of the abscissas; b—solid line denotes the density profile in the OA direction; the abscissa coordinate is measured from the focal point O.

CONCLUSION

The results given in this paper thus permit us to make an unambiguous interpretation of the physical phenomena accompanying the effect of a high-power laser pulse on the surface of a solid. Enhanced time resolution obtained through multiframe photography with laser illumination made it possible to record the high-temperature portion of the vaporized material and to determine the main parameters of hot plasma: the density distribution, the limiting velocity of plasma expansion, and the total mass. The last quantity is in satisfactory agreement with numerical calculations based on (5), (10) and (11) and also with the results of previous measurements. The experimentally determined maximum plasma temperature as a function of the radiation

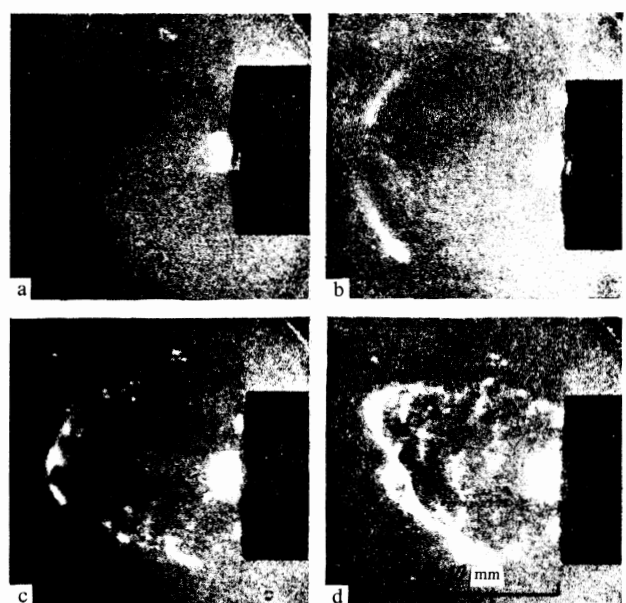


FIG. 12. Schlieren photographs of shock wave and flare at various pressures of residual gas in the chamber. Frames a, b, c, and d correspond to the pressures of 2×10^{-2} , 1, 2, and 4 mm Hg respectively. Laser output pulse energy is 6 J.

¹⁾Under the same conditions the electron temperature in the flare measured from the emission spectra amounted to $\sim 130 \text{ eV}$ [4].

flux density is also in agreement with the theoretical formulas and allows us to compute the radiation flux density required to reach the given temperature^[1,4]. In particular the observation threshold for neutrons generated by thermonuclear reactions corresponds to a radiation flux of the order of 20 Gw under our experimental conditions. A selection of a suitable target geometry allowing for the utilization of shock wave cumulation effects may possibly facilitate the problem of producing thermonuclear plasma. A variant of such an experiment was discussed earlier^[1a].

In conclusion we note that the results of this paper are of interest in the design of experiments for the study of kinetic phenomena and thermodynamic properties of various materials at high temperatures. In particular we note the possibility to study hard-to-sublimate materials, for which a high vapor density is very difficult to obtain under laboratory conditions.

The authors thank V. A. Boiko, B. V. Kruglov, and V. I. Frolov for help in performing the experiments.

¹N. G. Basov, V. A. Boiko, V. A. Dement'ev, O. N. Krokin, and G. V. Sklizkov, Zh. Eksp. Teor. Fiz. 51, 989 (1966) [Sov. Phys.-JETP 24, 659 (1967)].

²D. W. Gregg and J. T. Scott, J. of Appl. Phys. 38, 1729 (1967).

³O. V. Bogdankevich, V. Yu. Sudzilovskii, and A. A. Lozhnikov, Zh. Tekh. Fiz. 35, 2052 (1965) [Sov. Phys.-Tech. Phys. 10, 1573 (1966)].

⁴N. G. Basov, V. A. Boiko, Yu. N. Voinov, E. Ya. Kononov, S. L. Mandel'shtam, and G. V. Sklizkov, ZhETF Pis. Red. 5, 177 (1967); 6, 849 (1967) [JETP Lett. 5, 141 (1967)].

⁵Yu. A. Bykovskii, V. I. Dorofeev, V. I. Dymovich, B. I. Nikolaev, S. V. Ryzhikh, and S. M. Sil'nov, Zh. Tekh. Fiz. (1967), in press.

⁶Yu. F. Afanas'ev, V. M. Krol', O. N. Krokin, and I. V. Nemchinov, PMM 6 (1966).

⁷Yu. F. Afanas'ev and O. N. Krokin, Zh. Eksp. Teor. Fiz. 52, 966 (1967).

⁸O. N. Krokin, Zh. Tekh. Fiz. 34, 1324 (1964) [Sov. Phys.-Tech. Phys. 9, 1024 (1965)].

⁹O. N. Krokin, Zs. Angew. Mat. und Phys. 16, 123 (1965).

¹⁰I. V. Nemchinov, PMM 31, 300 (1967).

¹¹A. I. Pavlovskii and G. V. Sklizkov, PTÉ 2, 98 (1962).

¹²S. A. Akhmanov, A. I. Kovrigin, A. S. Iskarskas, and R. V. Khokhlov, ZhETF Pis. Red. 2, 223 (1965) [JETP Lett. 2, 141 (1965)].

¹³Yu. E. Nesterikhin and R. I. Soloukhin, Metody skorostnykh izmerenii v gazodinamike i fizike plazmy (High-speed Measurement Methods in Gas Dynamics and Plasma Physics), Izd. Nauka, 1967, chapter 6.

¹⁴N. G. Basov, O. N. Krokin, and G. V. Sklizkov, ZhETF Pis. Red. 6, 683 (1967) [JETP Lett. 6, 168 (1967)].

¹⁵Ya. B. Zel'dovich, Akustich. zh. 2, 28 (1956); Yu. P. Raizer, PMTF 1, 57 (1963).

¹⁶Ya. B. Zel'dovich and Yu. P. Raizer, Fizika udarnykh voln i vysokotemperaturnykh gidrodinamicheskikh yavlenii (Physics of Shock Waves and High-Temperature Hydrodynamic Phenomena), Izd. Nauka, 1966, chapter II, par. 22.

¹⁷S. I. Anisimov, A. M. Bonch-Bruevich, M. A. El'yashevich, Ya. A. Imas, I. A. Pavlenko, and G. S. Romanov, Zh. Tekh. Fiz. 36, 1273 (1966) [Sov. Phys.-Tech. Phys. 11, 945 (1967)].

¹⁸L. I. Sedov, Metody podobiya i razmernosti v mehanike (Methods of Simulation and Dimensionality in Mechanics), Gostekhizdat, 1957.

¹⁹G. G. Dolgov and S. L. Mandel'shtam, Zh. Eksp. Teor. Fiz. 24, 691 (1953).

²⁰R. Ladenburg, C. C. Van Voorhis, and J. Winckler, Phys. Rev. 76, 662 (1949). F. D. Bennett, W. C. Carter, and V. E. Bergdolt, J. Appl. Phys. 23, 453 (1952).

²¹N. M. Kuznetsov, Termodinamicheskie funktsii i udarnye adiabaty vozdukh pri vysokikh temperaturakh (Thermodynamic Functions and Shock Adiabats of Air at High Temperatures), Mashinostroenie, 1965.

Translated by S. Kassel
126